International Journal on Magnetic Particle Imaging
Vol 4, No 1, Article ID 1804001, 9 Pages

Infinite Science Publishing

Research Article

Modeling the Impedance of Water-Cooled Core-Less Multi-Layered Solenoid Coils for MPI Drive Field Generation

Christian Kuhlmann[a,*] · Sebastian Draack[a] · Thilo Viereck[a] · Meinhard Schilling[a] · Frank Ludwig[a]

[a]Institute of Electrical Measurement and Fundamentals of Electrical Engineering, Technische Universität Braunschweig, 38106 Braunschweig, Germany
*Corresponding author, email: c.kuhlmann@tu-bs.de

Received 11 November 2017; Accepted 14 January 2018; Published online 25 April 2018

Abstract

A complete lumped component model representing the wideband impedance of water-cooled multi-layered core-less solenoid coils is presented and analytical and numerical calculation methods for model elements are reviewed and extended. The model includes stray capacitances, mutual inductances and frequency-dependent resistive losses. Contrary to previous treatments of this topic, the model is not simplified further and is evaluated in its complete form, allowing accurate prediction of the coil impedance beyond the first resonant frequency. This aspect is especially important if the coil is part of a passive filter circuit, where higher resonances limit the filter bandwidth. Also, a liquid coolant is included in the calculations. Additionally, figures of merit for the evaluation of field homogeneity inside the coil are given. The model is applied to a MPI drive coil and is compared to measured data. It shows good agreement up to 4 MHz, including the second series resonance of the coil. Additionally, the influence of water-cooling on the coil impedance is investigated. Comparison of model results to measured data shows additional losses.

I. Introduction

Parasitic effects have a large impact on the high frequency behavior of coils. From the first resonant frequency onward, the coil impedance is dominated by the interaction of parasitic capacitances, mutual- and self inductances of individual turns, as well as frequency-dependent loss mechanisms such as skin- and proximity effect.

For the optimization of passive filter circuits, coil behavior beyond the first resonant frequency is important, because (higher) resonances often limit the bandwidth over which the filter maintains the desired response. Since Magnetic Particle Imaging (MPI) [1] drive field coils, which are used for field generation in the kHz range, are always a part of the transmit filters [2, 3], these resonances are an important design consideration.
This influence on the filter bandwidth happens because either the first (parallel) resonance or the second (series) resonance of the coil introduces an undesired pair of poles or zeros (respectively) into the coil's impedance, leading to deviations from its ideal characteristic. Since common filter synthesis assumes that coils only exhibit an impedance zero at the origin [4], the response of the filter deviates from the intended transfer function. For the bandpass and bandstop filters used in MPI, this results in limited attenuation at high frequencies or a limited maximum pass-band range respectively. Prediction of coil parameters before construction can therefore reveal whether these effects will limit scanner performance and

if a different construction or filter synthesis is advised.

Previous publications have established a lumped component coil model [5, 6] and provided a procedure to iteratively simplify it to extract the total capacitance value [7]. Additionally, numerical [8] and analytical [5–7] methods for the calculation of stray capacitances have been suggested. For electromagnetic compatibility (EMC) applications, the partial element equivalent circuits (PEEC) method [9] shows good agreement with measured data [10]. Although it provides good insight into the problem, field solvers using this method are not generally available for non-planar geometries. Also, to the knowledge of the authors, it has not been demonstrated for multi-layered coils or coils in dielectric media other than air. From a design perspective, it can be beneficial to let simulation elements coincide with the elements of the designed geometry, so that cell results directly correspond to design parameters.

This paper presents a method to predict the impedance and homogeneity of a multi-layered coreless solenoid coil over a wide frequency range, using analytical formulas or finite element method (FEM) data in combination with a SPICE circuit solver [11]. The simplifications compared to a full PEEC simulation in combination with analytic element estimation allow faster simulation times and good scaling, making it suitable for initial design verification and iterative optimization techniques. Unlike previous works, where individual circuit elements were removed from the network before solving it (e.g. the mutual inductance was added to the self-inductance [7]), the proposed method works beyond the first resonant frequency since it includes the interactions between individual windings. Additionally, we investigate the influence of water cooling (i.e. coil windings submerged in water) on the coil's impedance and the self resonant frequency, which has not been addressed before. The method was used to study the behavior of a MPI drive coil. Comparison of simulation results with measured data shows good agreement up to the second series resonance.

II. Methods

Computational electromagnetic methods are routinely used nowadays for the design of coils. However, if parasitic properties of the coil need to be determined, the complexity of the required computation rises. If the size of the structure is well below the wavelengths at the frequency range of interest, a lumped component model can be assembled to represent the problem. After determining individual element values, the lumped model can be solved instead, which is usually less computational intensive than a (full wave) EM simulation. It can also be combined with other component models, e.g. to predict the behavior of complete filter structures. To adequately represent a coil up to and beyond the first resonant frequency, the mutual and self inductance of the windings, as well as stray capacitances between them need to be considered. Also, frequency-dependent losses need to be modeled. When determining element values, it can be beneficial to use analytical formulas, especially in early design phases when fast verification of design intent is more important than high accuracy.

It should be noted that at frequencies where the current paths are significantly altered by displacement currents, the modeling of the magnetic coil properties needs to take these into account. To continue using a lumped component model, a smaller cell size as well as additional inductances are required and the element values become frequency dependent, which is beyond the scope of this work. Another limit appears once the wavelengths are of the same order as the size of the structures, so that retarded fields need to be modeled. From that frequency onward, full wave or full PEEC simulations are more adequate. For the frequency range of interest in MPI drive field applications, which is in the 10 kHz to 150 kHz range, field retardation is not required for structures with dimensions below several hundred meters. Even for MPI receive circuitry, which uses frequencies up to ≈ 2 MHz, lumped components models are usually sufficient for the geometries encountered in typical MPI scanners. At these frequency ranges the presented method is easier to apply than full wave simulations that struggle with the large span of geometric feature sizes in MPI coils. It also gives more accurate results than first order models that cannot predict higher coil resonances.

II.I. RLC Model for Quantitative Comparison

Figure 1 shows a commonly used RLC model that represents the whole coil including its first (parallel) resonance. We will use it to compare the results of a more sophisticated model network with measured data quantitatively. It includes the coil's inductance L_S, models its first parallel resonance through capacitance C_P, includes the coil's DC resistance through series resistance R_S (because usually $R_S \parallel R_P \approx R_S$) and the quality factor of the resonance by introducing a parallel resistance R_P (cf. [12]). Although higher order models are available, fitting these to measured data becomes increasingly ambiguous because several combinations of model parameters can yield the same residual sum of quadratic errors, which makes these higher order models unsuitable for parameter comparison.

II.II. Modeling Stray Capacitances Analytically

Several approaches have been presented to calculate the mutual capacitance of individual solenoid coil windings.

10.18416/ijmpi.2018.1804001

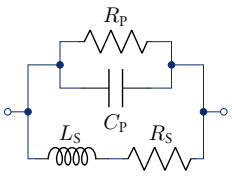

Figure 1: Simple RLC model of a coil that includes the inductance L_S, the first parallel resonance through capacitance C_P, DC resistance R_S and quality factor of the resonance R_P (cf. [12]).

All techniques assume that the winding radius R of the coil is much larger than the wire radius r_{cu} and neglect the curvature. In the following we want to denote the turn-to-turn capacitance between neighboring wires of the same layer as C_{tt} and distinguish it from the inter-layer capacitance C_i between windings of different layers.

Different assumptions have been made considering the effect of the opposite winding pitch of adjacent layers in a multi-layered coil: While *Massarini* et al. [5] assumed densely packed windings with a staggered pattern, *Hole* et al. [7] declared that adjacent layers will stack without shift due to the opposing pitch. Geometrical considera-

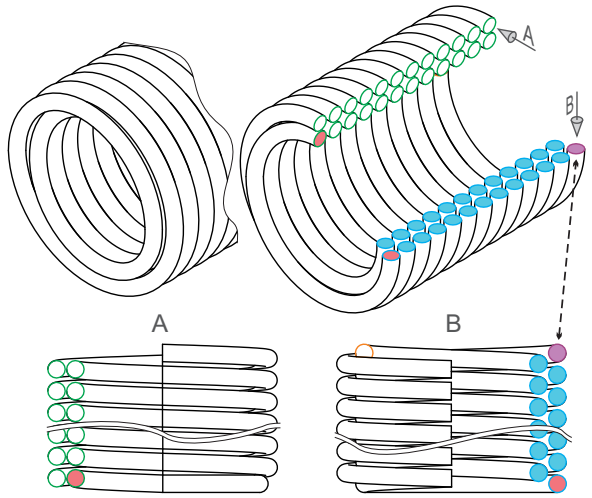

Figure 2: Cross sectional patterns of windings observed in multi-layer solenoid coils with layers of opposed pitch. The red filled winding makes the transition from the inner to the outer layer.

tions suggest that both variants appear: since a densely wound coil has a pitch of $2r_{cu}$ per turn, adjacent layers with opposite pitch will show the same cross-sectional pattern after every 180°, so both patterns alternate every 90° (cf. Figure 2).

To calculate the capacitance value, we have expanded the method proposed by *Massarini* et al. [5] to support spacing between wires. This allows us to use this approach for both winding patterns and incorporate manufacturing tolerances. We also incorporated surrounding dielectrics other than air. Similar to the original derivation we consider the series connection formed by the wire and the insulating coating with the ambient medium to another insulated wire. In the case where litz wire is used, it assumes that the thickness of the wire serving and the gap size between the wires are large compared to size of individual wire strands and therefore the deviations from the round shape can be neglected. Due to the symmetric nature of the arrangement, it is sufficient to calculate the capacitance of one half and account for the series arrangement. Figure 3 shows two adjacent windings with the associated dimensions and material properties.

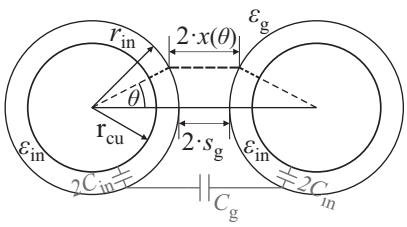

Figure 3: Geometrical arrangement of two adjacent windings and associated capacitances (cf. [5]). C_{in} is the total insulation capacitance between the wires and needs a factor of 2 if split into individual contributions. C_g is the capacitance formed by the gap between the wires. See text for other parameters.

The capacitance per differential angle of the series connected cylindrical capacitors formed by the wires and their insulation can be calculated through a conformal mapping as [5]

$$dC_{in} = \frac{\varepsilon_{in} l_t}{2\ln\left(\frac{r_{in}}{r_{cu}}\right)} d\theta, \tag{1}$$

where $l_t = 2\pi R$ is the turn length, r_{cu} is the wire radius, ε_{in} is the dielectric constant for the insulation material and r_{in} its outer radius.

C_{in} is in series with the capacitance C_g of the gap between two wires. Following the simplifications of *Massarini* et al., we assume that the electric field lines form straight connections between the wires. This assumption is adequate if the angular segment is small and the wires are densely packed. For each differential angle, using the basic capacitor formula with the differential surface element dS, we arrive at

$$dC_g = \varepsilon_g \frac{dS}{2\,x(\theta)} = \frac{\varepsilon_g\, l_t}{2} \frac{r_{in}}{s_g + r_{in}(1-\cos\theta)} d\theta. \tag{2}$$

Here, ε_g is the dielectric constant of the space between the wires, which are separated by a distance of $2s_g$. The expression for $x(\theta)$ follows from the geometry shown in Figure 3.

The total capacitance follows from the series connection of the segments.

$$dC_{\mathrm{ser}} = \frac{dC_{\mathrm{in}}\, dC_{\mathrm{g}}}{dC_{\mathrm{in}} + dC_{\mathrm{g}}} = \frac{1}{2}\frac{\varepsilon_{\mathrm{g}} l_t\, d\theta}{\frac{\varepsilon_{\mathrm{g}}}{\varepsilon_{\mathrm{in}}}\ln\left(\frac{s_{\mathrm{in}}}{r_{\mathrm{cu}}}\right) + \frac{s_{\mathrm{g}}}{r_{\mathrm{in}}} + 1 - \cos(\theta)}. \quad (3)$$

It includes the contributions of the insulations of both wires and the space between them. By integrating along the angle θ we arrive at an expression for the capacitance between two adjacent windings

$$C_{\mathrm{ser}} = \frac{l_{\mathrm{t}}\, r_{\mathrm{in}} \varepsilon_{\mathrm{g}} \varepsilon_{\mathrm{in}} \arctan\left(\frac{\left(\left(s_{\mathrm{g}}+2r_{\mathrm{in}}\right)\varepsilon_{\mathrm{in}}+D\right)\sin(\theta)}{(1+\cos(\theta))S}\right)}{S} \quad (4)$$

$$S = \sqrt{\left(s_{\mathrm{g}}+2r_{\mathrm{in}}\right)s_{\mathrm{g}}\,\varepsilon_{\mathrm{in}}{}^2 + \left(s_{\mathrm{g}}+r_{\mathrm{in}}\right)2\varepsilon_{\mathrm{in}}D + D^2} \quad (5)$$

$$D = \varepsilon_{\mathrm{g}} r_{\mathrm{in}} \ln\left(\frac{r_{\mathrm{in}}}{r_{\mathrm{cu}}}\right) \quad (6)$$

and evaluating this for an angle $\theta = \pm\frac{\pi}{6}$ (cf. [5]) results in

$$C_{\mathrm{tt}} = 2\left[C_{\mathrm{ser}}\right]_{\theta=0}^{\theta=\frac{\pi}{6}} = \frac{2\, l_{\mathrm{t}}\, r_{\mathrm{in}}\, \varepsilon_{\mathrm{g}}\, \varepsilon_{\mathrm{in}} \arctan\left(\frac{\varepsilon_{\mathrm{in}}\, s_{\mathrm{g}}+2\,\varepsilon_{\mathrm{in}}\, r_{\mathrm{in}}+D}{\left(\sqrt{3}+2\right)S}\right)}{S}. \quad (7)$$

Since it includes spacing and an intermediate medium, the same formula was used to calculate the inter-layer capacitance C_{i}.

II.III. FEM Modeling of Capacitances

The capacitance between adjacent wires can be calculated numerically by using finite element methods. To calculate the coupling capacitances to all neighboring wires efficiently, the potential of a wire n is changed by a small value ΔV_n compared to a reference simulation. For each adjacent wire m, the charge variation ΔQ_m is determined, while all wires except n are held at a constant potential. The individual coupling capacitances can be calculated by

$$C_{\mathrm{tt},m,n} = -\left.\frac{\Delta Q_m}{\Delta V_n}\right|_{V_m=\mathrm{const}}. \quad (8)$$

To get a quick result of the total capacitance of the coil that forms the first resonance with the coil's inductance, the complete structure can be simulated at once. Each wire should be assigned with a potential according to its position in the winding process (e.g. by assuming a unit voltage drop V_{coil} over the coil and a constant voltage drop per winding). The capacitance can be calculated by evaluating the total electrostatic energy E_E in the structure according to

$$C = \frac{2E_{\mathrm{E}}}{{V_{\mathrm{coil}}}^2}. \quad (9)$$

For the calculations in this work the open source FEMM (Finite Element Method Magnetics) package [13] has been used. Alternatively, many similar programs are available for this task.

II.IV. Analytical Modeling of Self- and Mutual Inductance

To calculate the self-inductance of the wires we rely on the well-known formula [14, 15] for the inductance of a wire loop

$$L_m = \mu_0 R\left(\ln\left(\frac{8R}{r_{\mathrm{cu}}}\right) - 2 + \frac{Y}{2}\right) \quad (10)$$

where μ_0 is the vacuum permeability, R is the coil radius and Y is a parameter that accounts for the current distribution in the wire. It is 0 when assuming surface currents and $\frac{1}{2}$ for a homogeneous current density across the wire cross section.

The mutual inductance between two coaxial wire loops m and n with the radii R_m, R_n and the positions z_m, z_n on the common axis, can be calculated using *Maxwell*'s formula [14, 16]

$$M_{m,n} = 4\pi\sqrt{R_m R_n}\left(\left(\frac{2}{k} - k\right)F_k - \frac{2}{k}E_k\right) \quad (11)$$

$$k = \frac{2\sqrt{R_m R_n}}{\sqrt{(R_m + R_n)^2 + (z_m - z_n)^2}} \quad (12)$$

where F_k and E_k are the complete elliptic integrals of the first and second kind respectively. It should be noted that many numerical implementations of these integrals expect k^2 as argument.

II.V. FEM Modeling of Self- and Mutual Inductances

Similar to the capacitance calculations, the mutual inductance can be determined numerically by evaluating the change in flux linkage $\Delta\Phi_m$ in a winding m in comparison to a reference value, as a result of a small change in current Δi_n in another winding n

$$M_{m,n} = \left.\frac{\Delta\Phi_m}{\Delta i_n}\right|_{i_m=\mathrm{const}}, \quad L_m = \frac{\Delta\Phi_m}{\Delta i_m}. \quad (13)$$

The coupling coefficient is calculated as

$$k_{M(m,n)} = \frac{M_{m,n}}{\sqrt{L_m L_n}} \quad (14)$$

II.VI. Predicting Coil Losses

Frequency-dependent coil losses can either be extracted from the real part of the coil voltage drop as predicted by the magnetic FEM simulation from the previous section, or can be calculated analytically. *Reatti* and *Bartoli* et al. [17, 18] have developed an analytical expression for the AC resistance of solid and litz wire solenoids. For litz wire they arrive at

$$R_{ac} = R_{dc}\frac{\gamma_s}{2}\left[\frac{1}{n_s}\frac{ber\gamma_s\, bei'\gamma_s - bei\gamma_s\, ber'\gamma_s}{ber'^2\gamma_s + bei'^2\gamma_s} + \left\{(-2\pi)\left(4\frac{{N_L}^2-1}{3}+1\right)n_s\left({\eta_1}^2+{\eta_2}^2\frac{p}{2\pi n_s}\right)\cdot\frac{ber_2\gamma_s\, ber'\gamma_s + bei_2\gamma_s\, bei'\gamma_s}{ber^2\gamma_s + bei^2\gamma_s}\right\}\right], \quad (15)$$

where $R_{dc} = \frac{4N_t l_t}{n_s\sigma\pi {d_s}^2}$ is the DC resistance, N_t is the total number of turns, l_t the (average) length of a single turn, n_s is the strand count of the litz wire, d_s a single strand's conductor diameter and σ its conductivity. $\gamma_s = \frac{d_s}{\delta\sqrt{2}}$, $\delta^{-1} = \sqrt{\pi f\mu_0\mu_r\sigma}$ is the skin depth, f the frequency and $\mu_0\mu_r$ the permeability of the strands. N_L is the layer count, $\eta_1 = \frac{d_o\sqrt{\pi}}{2t_o}$ the external porosity factor, $\eta_2 = \frac{d_s\sqrt{\pi}}{2t_s}$ the internal porosity factor, d_o the outer diameter of the litz wire bundle (without serving), t_o the distance between adjacent windings, t_s the spacing between strands, and $p = N_t\frac{{d_s}^2}{{d_o}^2}$ is the litz wire packing factor. The porosity factors closely resemble filling factors. The internal porosity factor refers to the packing of strands in the litz bundle while the external porosity factor describes the arrangement of adjacent litz wires. $ber_\nu z, bei_\nu z$ are the Bessel-Kelvin functions of argument z and order ν ($\nu = 0$ where omitted).

For the derivatives of the *Kelvin* functions, it is convenient to use the following identities [19]:

$$ber'_\nu z = \frac{-ber_{\nu-1}z + ber_{\nu+1}z - bei_{\nu-1}z + bei_{\nu+1}z}{2\sqrt{2}} \quad (16)$$

$$bei'_\nu z = \frac{+ber_{\nu-1}z - ber_{\nu+1}z - bei_{\nu-1}z + bei_{\nu+1}z}{2\sqrt{2}} \quad (17)$$

II.VII. Figures of Merit for Field Homogeneity

Salmon et al. [20] list several criteria for defining inhomogeneity. For MPI applications, the peak-to-peak field deviation IH_{pp} is the most critical value and should therefore be used for design evaluation:

$$IH_{\mathrm{pp}} = \frac{\max_{\vec{r}}\left(\vec{B}_{(\vec{r})}\cdot\vec{e}_s\right) - \min_{\vec{r}}\left(\vec{B}_{(\vec{r})}\cdot\vec{e}_s\right)}{\left|\vec{B}_{(\vec{r}_c)}\cdot\vec{e}_s\right|} \quad (18)$$

where $\vec{e}_s$ is the desired field direction and $\vec{B}_{(\vec{r}_c)}$ the field at the center of the FOV. The vector $\vec{r}$ should be evaluated over the complete volume of interest (VOI).

In addition, we propose the directional inhomogeneity as another figure of merit that is useful for MPI applications. For systems with multiple drive field axes, the angle of the field of an axis should be evaluated in addition to its mere projection into the axes direction. Again, we prefer to use a maximum deviation over average or root-mean-square (*rms*) values. We define the directional inhomogeneity IH_{DirMax} as

$$IH_{\mathrm{DirMax}} = \max_{\vec{r}}\left\{\arccos\left(\vec{B}_{(\vec{r})}\cdot\vec{e}_s\right)\right\}\frac{180^\circ}{\pi}. \quad (19)$$

II.VIII. Equivalent Circuit Model and Network Solution

Figure 4 shows the equivalent circuit model we used to represent the distributed parasitics of the coil, which is loosely based on the work of *Grandi* et al. [6]. Its central building block are the inductances of the individual windings L_m. To account for losses, we added the frequency-dependent resistors R_{ac} as well as regular resistors R_P parallel to the stray capacitances. Although it is reasonable to assume that these losses are frequency dependent as well in the case of a water cooled coil, there is no established model for these losses. While there are many works on the real part of the dielectric constant of water [21], there seems to be no equivalent for dielectric loss tangent in the kHz range. However, extending the model in such a way is easily accomplished, as the technique is the same as for R_{ac}. The lossy capacitors

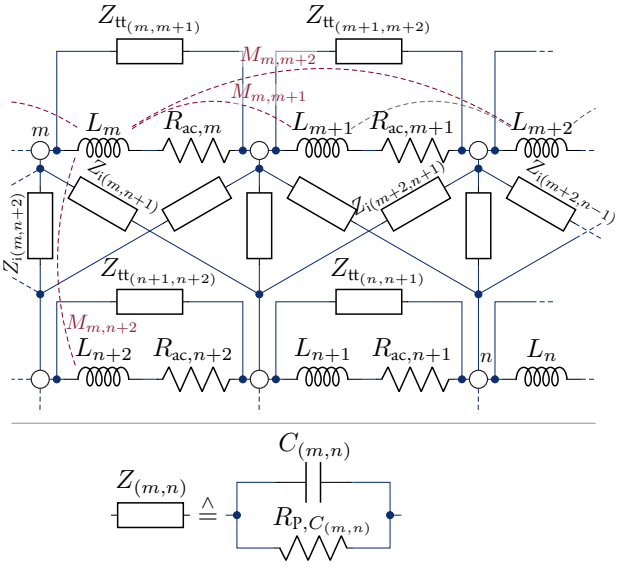

Figure 4: Lumped circuit model of a coil including parasitics. Indices m, n respect the winding direction of the corresponding layers.

are added between adjacent turns within the same layer (Z_{tt}) and between neighboring turns of adjacent layers (Z_{i}). Since the coil in our case is not in proximity to a shielding structure, winding-to-shield capacitances are not included in Figure 4. For the FEM simulations, a shield can be easily modeled if required and incorporated into the model. Analytical calculation methods for wire-to-shield capacitances are given by *Hole* et al. [7].

The (direct) stray capacitance between non-neighboring wires was neglected after FEM simulations predicted it consistently more than two orders of magnitude below the value of adjacent wires, owing to the distance as well as a shielding effect of the wire in between.

To accurately predict the coil impedance it is necessary to preserve the complete network structure, since higher resonances result from the complex interaction between stray capacitances and (mutual) inductances. Solving the network can either be performed by implementing a modified nodal approach [22], or by converting it into a net-list and using a SPICE [11] circuit solver. The latter approach has the additional benefit of directly implementing a simulation model of the coil that can be used in combination with other components, e.g. to simulate the behavior of complete filter circuits.

To account for the mutual inductances, a current controlled voltage source is added in series to the inductances of the windings. In the frequency domain, the induced voltage V_M in wire m as a result of the current changes in the other N windings n can be calculated from the branch voltages $V_{L,n}$ across the corresponding inductors L_n through

$$V_{M,m} = \sum_{\substack{n=1,\\ n\neq m}}^{N} \frac{M_{m,n}}{L_n} V_{L,n}. \tag{20}$$

However, if the SPICE program offers dedicated syntax to express coupling coefficients $k_{M(m,n)}$, this approach is favored, to allow the circuit solver to optimize its matrix. Adding a voltage source for each mutual inductance (as opposed to adding a voltage source that is dependent on the derivatives of multiple node currents) should be avoided as it dramatically increases the node count of the circuit. Even though the resulting network equations will be the same (if the matrix is simplified), this will severely slow down the circuit analysis step that assembles the network matrices.

III. Results

III.I. MPI Drive Coil Design

The previously described modeling methods and figures of merit were applied to optimize a MPI drive field generator for the use in a dual-frequency scanner in a series resonant circuit. A genetic algorithm [23, 24] was used to find a compromise between homogeneity, power losses, compact size and achievable field strength per unit current. An even layer count was favored to allow close proximity of the connecting wires.

As a result of the optimization, the cross section of the windings was arranged as a circle segment. To allow for a large radius of this circle and thus a compact design, additional windings (called reinforcement windings in Tab. 1) were added at either ends of the coil. The effect of these windings and the bend shape is that the homogeneity within the center region is better than for a straight solenoid coil of the same length. This allows easier access to the FOV (compared to longer coils) and reduces coil losses. Tab. 1 shows key data of the design.

Parameter	Value
Total winding count	180
Reinforcement windings	5 on each end
Layers	3 (+1 reinforcement)
Inner coil diameter (min)	47.1 mm
Coil bend radius	875 mm
Coil length (winding area)	116.88 mm
Total wire diameter	2.03 mm
Wire serving	2×30 µm Mylar
Litz strands	420
Strand diameter	0.071 mm
Strand insulation	2.5 µm Polyurethane
Wire spacing	5 µm
$\varepsilon_{\text{in}} = \varepsilon_{\text{Mylar}} \approx \varepsilon_{\text{PUR}}$	3.5 ε_0
$\varepsilon_{\text{g}} = \varepsilon_{\text{H}_2\text{O}}$	79.678 ε_0
Field per unit current	1.667 mT A^{-1}
VOI for (18), (19)	20 mm × 20 mm
IH_{pp}	0.676%
IH_{DirMax}	0.235°

Table 1: Drive coil data

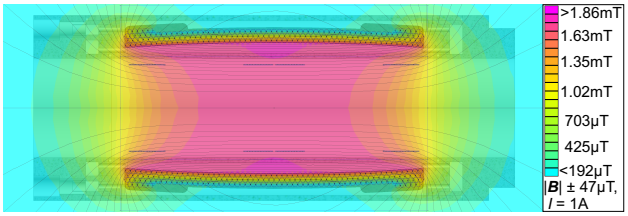

Figure 5: Drive coil design: CAD model with field overlay.

The coil was manufactured at the institute's workshop. The coil former is made of Polyamide 6. To direct the flow of the coolant, the top winding layers were sealed using a thin layer of epoxy casting resin.

III.II. Impedance Without Coolant

Impedance measurements of the completed coil were carried out using an *Agilent* 4294A impedance analyzer with a 42941A probe. Fig. 6 shows a comparison between the measured impedance data $Z_{\text{Meas.}}$ and the impedance as predicted by the lumped component model with element values calculated using the FEM simulation (Z_{FEM}), as well as the analytical formulas ($Z_{\text{Analyt.}}$).

As is apparent from Fig. 6, the impedance of the coil is reasonably well predicted by the network up to the second series resonance at 3 MHz. Frequency-dependent

losses, however, are overestimated from that point onward so that the quality factor of the second series resonance ($Q_{\mathrm{FEM,2^{nd}ser}} = 2.65$) is predicted lower than apparent from measured data ($Q_{\mathrm{Meas.,2^{nd}ser}} = 8.56$). For frequencies below the second series resonance the ac losses show better agreement with the measured resistance, although losses are slightly overestimated there as well ($Q_{\mathrm{FEM,2^{nd}par}} = 23.95$ vs. $Q_{\mathrm{Meas.,2^{nd}par}} = 24.69$). The losses were determined by taking the real part of the impedance and by evaluating the quality factors of the resonances. The measurement uncertainty of the Q factors should be below 4% for the settings used [25].

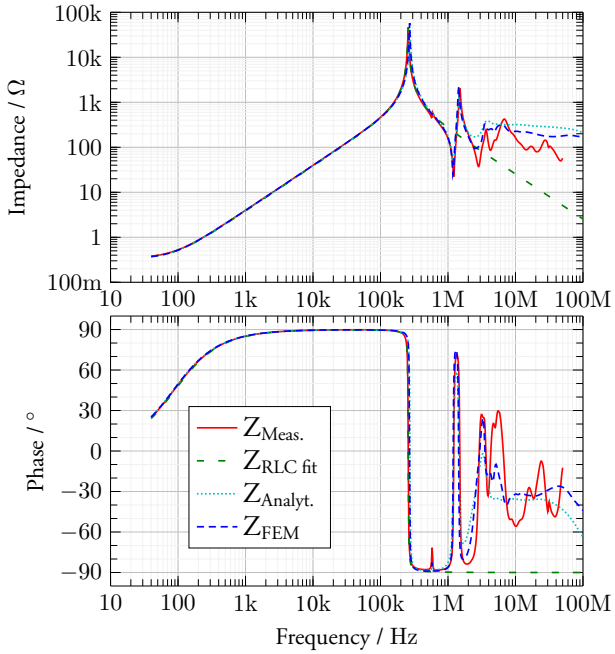

Figure 6: Predicted impedance through analytical calculations ($Z_{\mathrm{Analyt.}}$) and FEM simulations (Z_{FEM}) compared to the measured impedance ($Z_{\mathrm{Meas.}}$) of the coil in air. An RLC model fit ($Z_{\mathrm{RLC\,fit}}$) to measured data is shown as well.

Both analytical and FEM predictions show good agreement with measured data. To quantitatively compare the results with measured data, a RLC model (cf. Fig. 1) is fitted to both simulated and measured data and the resulting fit parameters are compared: The inductance value of the finite element simulation and the analytical formula show a −0.8 % and −0.2 % deviation from measured data respectively. Self-capacitance values show larger errors of −7.9 % and −11.0 % compared to measured results. As a consequence of the discrepancies, the self resonance is shown +4.6 % and +5.8 % too high by the models.

III.III. Water-Cooled Coil

Water-cooling of coils fabricated from litz wire is often a compromise between low impact on the self resonant frequency and low thermal resistance between the windings and the coolant. To reduce the influence on stray capacitances, coated wires can be used. For the example shown here, the litz wire was covered by two layers of Mylar serving. The insulation thickness is assumed to be 65 µm, which is in agreement with a measured thickness of 30 µm for a single Mylar foil layer. Experiments showed that the effect of the Mylar serving stems from its dielectric constant and not its tight sealing of the wires: Damaging the serving so that water can access the space between the strands (while keeping the serving mostly in place) only has minor influence on the self-capacitance of the coil.

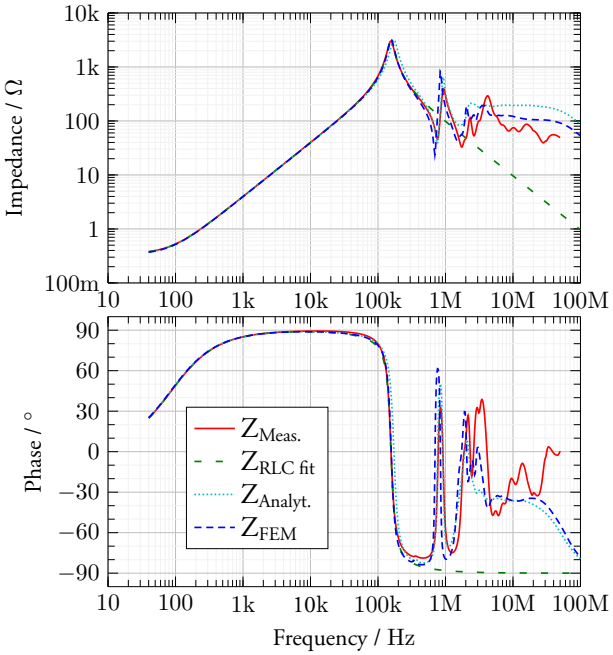

Figure 7: Predicted and measured impedance of the coil in water.

Fig. 7 shows the impedance prediction compared to measured data for the water cooled coil. Again, the measured data agree with the predicted values by the finite element method up to the second series resonance. The first self resonance shows very good agreement for the FEM data with +1.22% deviation, but larger errors for the analytical results (+10.9%). However, the frequencies of higher resonances are predicted 9% lower than actually measured. Another observation can be made from the quality factor of the higher resonances: Both analytical results and FEM values predict higher quality factors than those which are apparent from the measurement ($Q_{\mathrm{FEM,2^{nd}par}} = 16.75$ vs. $Q_{\mathrm{Meas.,2^{nd}par}} = 7.93$). This is in contrast to the slight over-prediction of losses that was found for the dry coil. A possible explanation for this behavior are losses from the coolant and additional proximity effect losses from displacement currents. The

deviations for the higher resonances may in part also be due to the changed current paths in the coil. Since the overall capacitances are much larger in the water cooled case, displacement currents are increased in that case.

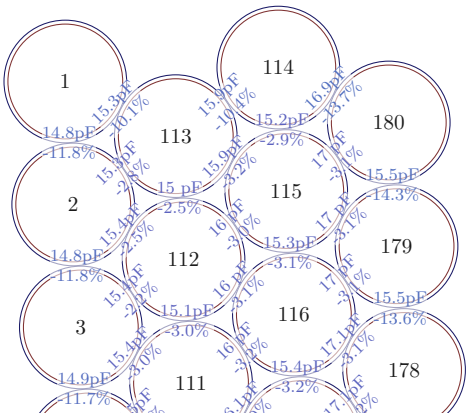

(a) Air

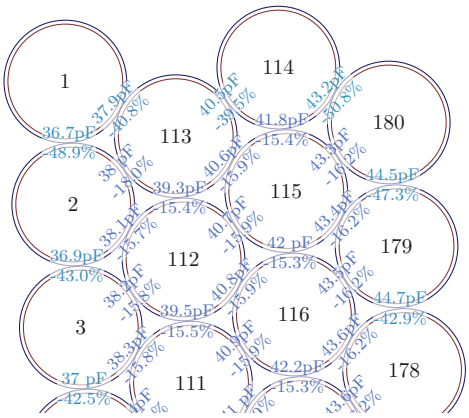

(b) Water

Figure 8: Analytical values compared to FEM reference results for individual windings for (a) the coil in air, (b) the water-cooled coil. The detail shows the upper end of the windings. Numbers without units indicate the windings order.

Comparing analytical results and FEM simulation data shows that the analytical formulas under-predict the capacitance between wires. Fig. 8 shows the analytically calculated values and the differences compared to FEM results for a detail of the coil. Values are positioned between the windings to which they correspond. Deviations are largest for windings at the edge of the winding area. This observation might allow future improvements in the analytical models to better account for media with high dielectric constants.

III.IV. Stacked winding pattern

Based on the work of *Hole* et al. [7], we also performed simulations where windings are stacked without staggering, similar to the green marked winding pattern in Fig. 2. However, the results of FEM simulations, as well as the analytical formulas for the capacitance [7], (8) show larger deviations (in the same direction) than the staggered pattern. It was found that the FEM results in water show acceptable agreement, but the self resonance for the dry coil is predicted too high (cf. Fig. 9).

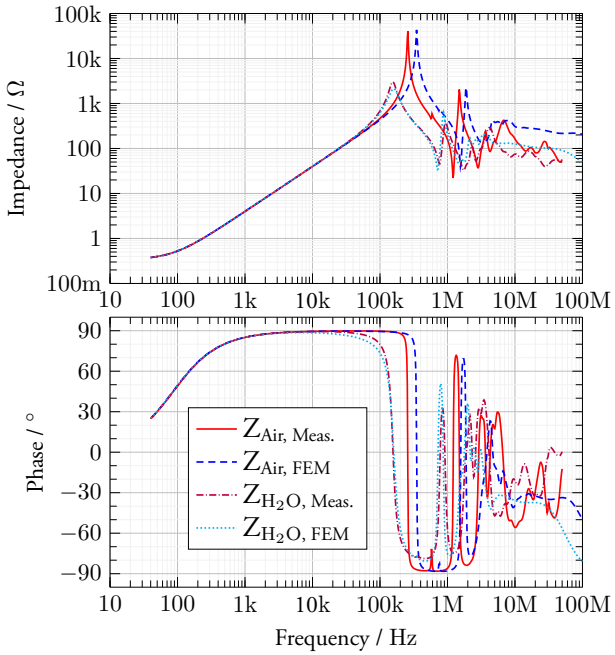

Figure 9: Predicted and measured impedance of the coil in water and air for the stacked winding pattern.

This can be explained through the fact that the stray capacitances for the water-cooled coil are dominated by the insulation and serving material's permittivity and thickness. Since the dielectric constant of water is very high ($\varepsilon_{\mathrm{H_2O}} = 79.678\,\varepsilon_0$) in comparison to that of most insulators, this offsets the larger spacing in the stacked configuration and the series connection of both capacitances is still dominated by the insulation. This is true in water for the chosen configuration up to a gap size $2s_g = 2.969\,\mathrm{mm}$ where both become equal with $C_g = C_{\mathrm{in}} = 36.28\,\mathrm{pF}$. The gap size plays a larger role in the dry case with C_g being smaller than 36 pF for gap sizes $2s_g > 10.5\,\mu\mathrm{m}$ and thus dominating the series connection even with tight spacing. Therefore, large deviations are observed in this case with the stacked pattern.

Apparently, the winding pattern of litz wire is better described by the staggered arrangement. Most likely this is in part due to the flexible nature of the used litz wire, which will tend to form closer spacings than solid wire would. Also, since the staggered pattern will always appear as well for opposing winding pitches, the parallel connection of both patterns will be governed by the larger contribution, which will always correspond to the staggered pattern.

10.18416/ijmpi.2018.1804001

IV. Conclusion

We have shown a practical method for predicting the impedance of liquid cooled multi-layered core-less solenoid coils by calculating the element values of a lumped component model and using the resulting network as a simulation model. Additionally, figures of merit for the field homogeneity of the coil were presented.

The proposed methods have been successfully used to construct a water-cooled drive-field coil for a dual-frequency MPI scanner. Measured values show generally good agreement with the coil models, even for higher resonances. This information is very beneficial when evaluating the frequency response of a complete MPI transmit chain, since parasitic resonances can limit the rejection bandwidth.

Limitations of the analytical models for the stray capacitances as well as additional loss mechanisms have been identified for the water-cooled case, giving room for future refinements and research.

Acknowledgment

Financial support by the DFG under grant no. LU 800/5-1 and SCHI 383/2-1 is gratefully acknowledged.

References

[1] B. Gleich and J. Weizenecker. Tomographic imaging using the nonlinear response of magnetic particles. *Nature*, 435:1214, 2005. doi:10.1038/nature03808.

[2] I. Schmale, B. Gleich, J. Kanzenbach, J. Rahmer, J. Schmidt, J. Weizenecker, and J. Borgert. An introduction to the hardware of magnetic particle imaging. In *IFMBE Proceedings*, pages 450–453. Springer Berlin Heidelberg, 2009. doi:10.1007/978-3-642-03879-2_127.

[3] T. Knopp and T. M. Buzug. *Magnetic Particle Imaging: An Introduction to Imaging Principles and Scanner Instrumentation*. Springer-Verlag GmbH, 2012. ISBN 3642041981.

[4] K. L. Su. *Analog Filters*. Springer, 2002. ISBN 1402070330.

[5] A. Massarini and M. K. Kazimierczuk. Self-capacitance of inductors. *IEEE Trans. Power Electron.*, 12(4):671–676, Jul 1997. ISSN 0885-8993. doi:10.1109/63.602562.

[6] G. Grandi, M. K. Kazimierczuk, A. Massarini, and U. Reggiani. Stray capacitances of single-layer solenoid air-core inductors. *IEEE Trans. Ind. Appl.*, 35(5):1162–1168, 1999. ISSN 0093-9994. doi:10.1109/28.793378.

[7] M.J. Hole and L.C. Appel. Stray capacitance of a two-layer air-cored inductor. *IEE Proceedings - Circuits, Devices and Systems*, 152(6):565, 2005. doi:10.1049/ip-cds:20045217.

[8] Q. Yu and T. W. Holmes. A study on stray capacitance modeling of inductors by using the finite element method. *IEEE Trans. Electromagn. Compat.*, 43(1):88–93, Feb 2001. ISSN 0018-9375. doi:10.1109/15.917948.

[9] A. E. Ruehli. Equivalent circuit models for three-dimensional multiconductor systems. *IEEE Trans. Microw. Theory Tech.*, 22(3):216–221, Mar 1974. ISSN 0018-9480. doi:10.1109/TMTT.1974.1128204.

[10] I. F. Kovačević, T. Friedli, A. M. Müsing, and J. W. Kolar. 3-D electromagnetic modeling of parasitics and mutual coupling in emi filters. *IEEE Trans. Power Electron.*, 29(1):135–149, Jan 2014. ISSN 0885-8993. doi:10.1109/TPEL.2013.2254130.

[11] L. W. Nagel. Spice2 : A computer program to simulate semiconductor circuits. *Ph. D. dissertation, University of California at Berkeley*, 1975.

[12] H. Haruta. *The impedance measurement handbook: a guide to measurement technology and techniques*. Agilent Technologies, 2000.

[13] K. B. Baltzis. The FEMM package: A simple, fast, and accurate open source electromagnetic tool in science and engineering. *J. Eng. Sci. Tech. Rev.*, 1:83–89, 2008.

[14] E. B. Rosa and F. W. Grover. Formulas and tables for the calculation of mutual and self inductance.(revised.). *J. Wash. Acad. Sci.*, 1(1/2): 14–16, 1911.

[15] R. Dengler. Self inductance of a wire loop as a curve integral. *ArXiv e-prints*, April 2012.

[16] J. C. Maxwell. *A Treatise on Electricity and Magnetism, third ed. Clarendon Press, Berlin*, volume II, chapter XIV. Circular currents. Clarendon Press, 1891.

[17] A. Reatti and F. Grasso. Solid and litz-wire winding non-linear resistance comparison. In *Proceedings of the 43rd IEEE Midwest Symposium on Circuits and Systems (Cat.No.CH37144)*, volume 1, pages 466–469 vol.1, 2000. doi:10.1109/MWSCAS.2000.951684.

[18] M. Bartoli, N. Noferi, A. Reatti, and M. K. Kazimierczuk. Modelling winding losses in high-frequency power inductors. *J. Circuits Syst. Comput.*, 05(04):607–626, 1995. doi:10.1142/S0218126695000370.

[19] M. Abramowitz and I.A. Stegun. *Handbook of Mathematical Functions with Formulas, Graphs, and Mathematical Tables*. A Wiley-Interscience publication. Wiley, 1972. ISBN 9780471800071.

[20] C. E. G. Salmon, E. L. G. Vidoto, M. J. Martins, and A. Tannús. Optimization of saddle coils for magnetic resonance imaging. *Braz. J. Phys.*, 36(1a), mar 2006. doi:10.1590/s0103-97332006000100004.

[21] D. P. Fernández, Y. Mulev, A. R. H. Goodwin, and J. M. H. Levelt Sengers. A database for the static dielectric constant of water and steam. *J. Phys. Chem. Ref. Data*, 24(1):33–70, 1995. doi:10.1063/1.555977.

[22] C.-W. Ho, A. Ruehli, and P. Brennan. The modified nodal approach to network analysis. *IEEE Trans. Circuits Syst.*, 22(6):504–509, 1975. ISSN 0098-4094. doi:10.1109/TCS.1975.1084079.

[23] P. N. Murgatroyd and D. P. Eastaugh. Optimum shapes for multilayered toroidal inductors. *IEE Proceedings - Electric Power Applications*, 147:75–81(6), 2000. ISSN 1350-2352.

[24] K. F. Man, K. S. Tang, and S. Kwong. Genetic algorithms: concepts and applications [in engineering design]. *IEEE Trans. Ind. Electron.*, 43(5):519–534, 1996. ISSN 0278-0046. doi:10.1109/41.538609.

[25] Agilent. *Agilent 4294A Precision Impedance Analyzer Data Sheet*. Agilent Technologies, Santa Rosa, CA, USA, 5968-3809e edition, 2008.

